In vivo fluorescence lifetime tomography

Ralph E. Nothdurft
Sachin V. Patwardhan
Walter Akers
Yunpeng Ye
Samuel Achilefu
Joseph P. Culver
Washington University School of Medicine
Department of Radiology
Mallinckrodt Institute of Radiology
St. Louis, Missouri 63110

Abstract. Local molecular and physiological processes can be imaged *in vivo* through perturbations in the fluorescence lifetime (FLT) of optical imaging agents. In addition to providing functional information, FLT methods can quantify specific molecular events and multiplex diagnostic and prognostic information. We have developed a fluorescence lifetime diffuse optical tomography (DOT) system for *in vivo* preclinical imaging. Data is captured using a time-resolved intensified charge coupled device (ICCD) system to measure fluorescence excitation and emission in the time domain. Data is then converted to the frequency domain, and we simultaneously reconstruct images of yield and lifetime using an extension to the normalized Born approach. By using differential phase measurements, we demonstrate DOT imaging of short lifetimes (from 350 ps) with high precision (±5 ps). Furthermore, this system retains the efficiency, speed, and flexibility of transmission geometry DOT. We demonstrate feasibility of FLT-DOT through a progressive series of experiments. Lifetime range and repeatability are first measured in phantoms. Imaging of subcutaneous implants then verifies the FLT-DOT approach *in vivo* in the presence of inhomogeneous optical properties. Use in a common research scenario is ultimately demonstrated by imaging accumulation of a targeted near-infrared (NIR) fluorescent-labeled peptide probe (cypate-RGD) in a mouse with a subcutaneous tumor. © *2009 Society of Photo-Optical Instrumentation Engineers.* [DOI: 10.1117/1.3086607]

1 Introduction

The fluorescence lifetime (FLT) of a fluorescent probe can be engineered to sense and report its local molecular environment. For example, fluorescence lifetime imaging microscopy (FLIM) methods have successfully employed FLT contrast to examine local biochemical properties (e.g., binding, polarity, and pH) independent of reporter concentration.[1] Despite the appeal of FLT contrast, concerted efforts to translate FLT methods from cells and phantoms to whole-body imaging of animals have been limited, likely due to the engineering challenges inherent to deep tissue *in vivo* imaging. This is particularly true for near-infrared (NIR) optical imaging that allows assessment of tissue beyond the superficial layer. Herein, we report the development of an NIR time-resolved fluorescence tomography platform for imaging small animals with simultaneous reconstructions of yield and lifetime. We outline design extensions from a previously reported time-resolved diffuse optical tomography (DOT) system,[2] evaluate the FLT-DOT performance, and demonstrate *in vivo* feasibility.

The *in vivo* environment places a number of requirements on FLT-DOT imaging systems. Foremost, fluorescence lifetimes range from 100 ps to greater than 5 ns (Ref. [3]) and

therefore require high-speed electro-optic measurement techniques. Furthermore, these time scales are on the same order as photon propagation in the tissue, and thus photon transit times in tissue must be explicitly accounted for.[4,5] To address these timing challenges, we choose to directly measure the phase difference [effectively, the difference in the mean time of flight (MTOF)] between the excitation light and the fluorescence emission. Previous frequency-domain FLT systems have been used to image phantoms but have had restricted data sets. We use a planar transmission geometry in order to maintain flat sampling throughout the subject,[6,7] to minimize moving parts, and to utilize lens-coupled detection.[8–10] The flat sampling has the additional benefit of greatly reducing superficial autofluorescence relative to reflectance imaging systems. Last, to provide efficient linear inverse solutions, we convert our measurement data to the frequency domain and adapt a normalized Born approach[11] for tomographic reconstructions of FLT.[4] We elaborate on these decisions and their alternatives in the following discussion.

The capabilities of the system are demonstrated through a combination of phantom testing and *in vivo* imaging. Phantoms with biologically equivalent optical properties provide a controlled assessment of the system's dynamic range and repeatability. Mice, which provide the initial mammalian model for many biological studies, are then examined in two experi-

Address all correspondence to Joseph Culver, Dept. of Radiology, Washington University in St. Louis, 4525 Scott Ave., East Bldg. Rm 1137, St. Louis, MO 63110. Tel: 314–747–1341; Fax: 314–747–5191; E-mail: culverj@wustl.edu
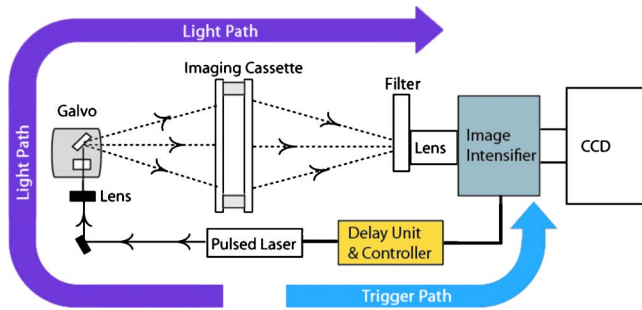
Fig. 1 Schematic of the temporally resolved fluorescence tomography system. A pulsed laser source is used for illumination. The system is configured to use a Ti:S laser with spectral filtering (80 MHz, 780 nm, <100-fs pulse width, 60 mW). The beam, after passing through the focusing lens, is steered by a pair of galvanometer scanning mirrors to the source side of the imaging cassette. Light emitted from the detector plane of the imaging cassette is filtered and collected by a lens and temporally gated (gate full width at half maximum=300 to 1600 ps) by an ultrafast gated image intensifier and detected by an EMCCD camera for read-out. Timing between the source and the gated detection is controlled by a trigger pulse received from the pulsed laser source, which is passed through a programmable delay unit to the ultrafast high-voltage image intensifier control.

ments. Subcutaneous implants first allow us to verify the reconstruction in the presence of *in vivo* confounds. We then examine a typical subcutaneous tumor preclinical cancer model. Here, we measure the lifetime of a targeted cypate-RGD probe in the tumor and liver regions.[12–14]

2 Methods and Materials

2.1 Fluorescence Lifetime Tomography System

2.1.1 Overview

The basic imaging configuration consists of a planar transmission geometry with a raster-scanned laser-illuminated *source* window and a lens-coupled camera profiling the light transmission on the opposing *detector* window (Fig. 1). An experiment consists of collecting two measurement sets. Within each measurement set, or *scan*, we illuminate each source and measure the output at each detector position as a function of time. An *excitation scan* consists of collecting a scan without spectrally filtering the light transmitted to the detector. An *emission scan* consists of collecting a scan with a spectral bandpass filter that rejects the excitation light and transmits the fluorescence emission. For reconstructing images, we use ratiometric data that is approximately equal to the ratio of the emission scan divided by the excitation scan. Details are provided in the following.

2.1.2 Hardware layout

Our illumination path begins with a mode-locked Ti:Sapphire (Ti:S) laser producing <100 fs pulses at 780-nm peak wavelength. This wavelength is reinforced by a 780-nm, 10-nm FWHM filter, resulting in a typical power of 60 mW. Neutral density filters allow reduction of intensity as necessary (e.g., for excitation scans). The beam is shuttered by a high-speed galvanometer (AO, Model 6210H, Cambridge Technology, Lexington, Massachusetts) with switching times <100 μs and then steered by a *x-y* galvanometer pair (AO, Model

6230, Cambridge Technology) to illuminate the imaging chamber at the desired location. This arrangement allows for flexible and dense spatial source positioning.

The present imaging chamber configuration has a 7×7 cm square window on each side. Window separation is adjustable to account for target thickness—typically, 1.6 cm. An adjustable gasket spans the distance between the two windows, allowing the chamber to be filled with optical matching fluid.

Light exiting the chamber passes through a filter-wheel before reaching the detector. Excitation scans are taken with neutral density filters to adjust the light levels to the dynamic range of the detector. Fluorescence emission scans are taken using an 830-nm, 10-nm FWHM, bandpass filter.

An ultrafast image intensifier (PicoStarHR-12, LaVision, Inc., Ypsilanti, Michigan) relays gated images of the light levels on the detection plane to an electron multiplying charged coupled device (EMCCD) camera (iXon 877f, Andor Technologies, South Windsor, Connecticut). Light transmitted through the tissue volume is temporally resolved using "comb" mode detection (see the following). This arrangement provides flexible and dense parallel detector sampling with a large field of view.

A MATLAB (R2007b, The Mathworks, Inc., Natick, Massachusetts) data acquisition program first initializes the system components and then queues a series of time-dependent commands to dedicated DAQ intermediaries. During acquisition, the PC stores frame-transferred images to a buffer in memory and subsequently to hard disk. The required number of images is the product of the number of source positions (dependent on scan area) and the number of time points desired for the intensity profile (12 for phantom imaging and 8 for *in vivo* imaging in the results presented herein).

2.1.3 Time-domain data acquisition in the "comb" mode

For clarity, we review how time resolution of the light pulse is achieved by operating the image intensifier synchronously with the pulsed source. The mode-locked Ti:S provides a series of <100-fs pulses at 80 MHz. A photodiode within the laser cavity provides an electrical pulse synchronously with each light pulse. The photodiode output is input to the delay unit, which generates an output pulse at a variable and programmable delay. The delayed output triggers the gated image intensifier. The image intensifier boosts the light transmitted from the target for a set period of time. (τ_{gate} can be programmed from 300 to 1600 ps; for the studies in this paper, we used $\tau_{gate}=800$ ps.) This gated transmission occurs for each pulse in a pulse train, or "comb" of pulses. The transmitted portions from many pulses (a 1-s train=$8*10^7$ pulses) then accumulate on the EMCCD, resulting in a measurement at every detection pixel for a set time point (time delay). The image is then read out from the camera at a much slower speed, >tens of millseconds. Incrementally increasing the time delay between the illumination comb and the detection comb and repeating the process results provides a temporal profile of the light intensity for each pixel.

2.1.4 *Conversion to frequency domain*

Fourier transformation of the time-domain data provides frequency-domain data from 200 MHz to 1.6 GHz (Refs. 2). The actual frequencies used depend on the number of time points measured and their combined time span. We define basis functions for the lowest frequency up to the Nyquist frequency. Reconstructions can employ any or all of these frequencies. For the experiments reported here, we use the lowest basis frequency. In phantoms, where we capture 12 data points in 400-ps steps, this is $\omega = 210$ MHz. For the *in vivo* scans, we capture 8 time points, making $\omega = 313$ MHz.

2.1.5 *Frequency-domain image reconstruction*

The generalized Born method serves as the basis for several tomographic reconstruction approaches.[4,11] Here, we expand on the method by combining simultaneous yield and lifetime reconstructions[4] with an explicit account of transmitted excitation.[11] In discrete notation, this normalized Born method takes the form $\mathbf{y} = \mathbf{Ax}$ with the following definitions:

$$y_i = \left[\frac{\Phi(\mathbf{r}_{s(i)}, \mathbf{r}_{d(i)}, \omega, \lambda_{emi}) - \theta_f \Phi_o(\mathbf{r}_{s(i)}, \mathbf{r}_{d(i)}, \omega, \lambda_{exc})}{\Phi_o(\mathbf{r}_{s(i)}, \mathbf{r}_{d(i)}, \omega, \lambda_{exc})} \right],$$

$$A_{i,j} = -S_o \frac{G(\mathbf{r}_{s(i)}, \mathbf{r}_j, \omega, \lambda_{exc}) G(\mathbf{r}_j, \mathbf{r}_{d(i)}, \omega, \lambda_{emi})}{G(\mathbf{r}_{s(i)}, \mathbf{r}_{d(i)}, \omega, \lambda_{exc})},$$

$$x_j = \frac{\eta_j}{1 - i\omega\tau_j}.$$

Here, $\mathbf{y}$ is the ratio of emission to excitation photon density $[\Phi(\mathbf{r}_{s(i)}, \mathbf{r}_{d(i)}, \omega, \lambda)]$ measured experimentally. Each measurement (indexed by i) is a function of the source location $[r_{s(i)}]$, detector location $[r_{d(i)}]$, modulation frequency (ω), excitation wavelength (λ_{exc}), and emission wavelength (λ_{emi}). An additional term, θ, in the numerator allows for compensation for emission filter bleed-through. From diffusion theory, we calculate $\mathbf{A}$, the influence of a particular voxel on every source and detector measurement. The two-point Green's functions, G, model light transport for given boundary conditions, optical properties, and the locations of sources, detectors, and voxels (r_j). In our case, a plane-parallel slab geometry is used.[15,16] S_o is a calibration factor. The reconstruction task is to solve for complex image voxels $(\mathbf{x_j})$. Here, we use the algebraic reconstruction technique (ART).[17] After reconstruction, the real (x_R) and imaginary (x_I) components of $\mathbf{x_j}$ are converted to $yield \equiv \eta = (x_R^2 + x_I^2)/x_R$ and $lifetime \equiv \tau = x_I/\omega x_R$.

2.2 *Image Subjects*

2.2.1 *Optical matching fluid*

We immerse our subjects in optical matching fluid to provide the plane-parallel slab geometry expected by the aforementioned reconstruction algorithms. The fluid's role is similar to that of ultrasound gel, but here we match the typical diffuse optical properties of the subject. Intralipid and india ink are added to deionized water to adjust the reduced scattering coefficient, μ_s', and absorption coefficient, μ_a, respectively. We

typically use a μ_s' between 5 cm^{-1} and 10 cm^{-1} and a μ_a between 0.1 cm^{-1} and 0.3 cm^{-1}. For phantoms presented here, the optical matching fluid has $\mu_s' = 5$ cm^{-1} and $\mu_a = 0.1$ cm^{-1}. For the *in vivo* experiments, we increase these values to $\mu_s' = 10$ cm^{-1} and $\mu_a = 0.2$ cm^{-1} to better match the optical properties of the mouse.

2.2.2 *Phantom precision and accuracy*

Our phantoms are 5-mm-diam disposable nuclear magnetic resonance (NMR) tubes (Fisher Scientific, Pittsburgh, Pennsylvania) filled with the combination of dye and media of interest. These are placed vertically in the center of the imaging chamber. Two phantom tubes were prepared, one with 1 μM IR820 (Sigma Aldrich, St. Louis, Missouri), where we expect a lifetime below 0.5 ns, and the other with 50 nM DTCCI (Sigma Aldrich), where we expect a lifetime above 1 ns. A band of sources (24 across and 3 vertically with 2-mm separation) was scanned for 12 time-gates. Excitation scans required 50 seconds, while emission scans took 4 minutes 40 seconds. To evaluate signal and noise levels, we alternated excitation and emission scans until a total of 15 scans of each type were acquired. The mean values and standard deviations for measurement were computed across the 15 scans.

2.2.3 *In vivo protocol*

Male nude mice 6 to 12 weeks in age were used for *in vivo* imaging. Prior to scanning, each mouse was anesthetized with a mixture of ketamine (87 mg/kg) and xylazine (13 mg/kg) via intraperitoneal and subcutaneous injection for initial and sustained sedation, respectively. The mouse was then suspended vertically within the fluid-filled imaging cassette for the duration of the scan, as previously described.[9] Mice were monitored visually for breathing. We have used this process for up to two hours at a time and have had no adverse issues.

For a controlled target in an *in vivo* background, gelatin disks 4 mm in diameter and 2 mm thick were made from 1% agarose gel. During production, the targets were loaded with the NIR dyes DTCCI and cypate. Cypate, a biologically compatible analog to the commonly used ICG with similar excitation and emission features (785-nm excitation, 820-nm emission), was synthesized and characterized as previously described.[18] The disk targets were implanted in mice approximately 3 mm below the skin surface in the subcutaneous space through a 5 mm incision on the dorsal aspect of each flank. Dye concentrations were chosen to produce similar fluorescence signal from both targets with 1 μM cypate and 0.2 μM DTCCI on the left and right flanks, respectively. Skin incisions were closed with tissue adhesive (Nexaband, Abbott Animal Health, North Chicago, Illinois) and the mouse was positioned for imaging. Eight time-gates over a 16-by-12 source grid with 3-mm separation were imaged, covering a total area of 4.8 cm $\times$ 3.6 cm. The acquisition time for the entire set of data was approximately 2 min for excitation and 11 min for emission.

To demonstrate *in vivo* lifetime reconstruction for a typical biological model, we imaged the biodistribution of an intravenously injected near-infrared fluorophore (NIRF) molecular probe. The NIRF molecular probe consisted of cypate conjugated to a cyclic RGD peptide (cyclo[RGDfK], where f is
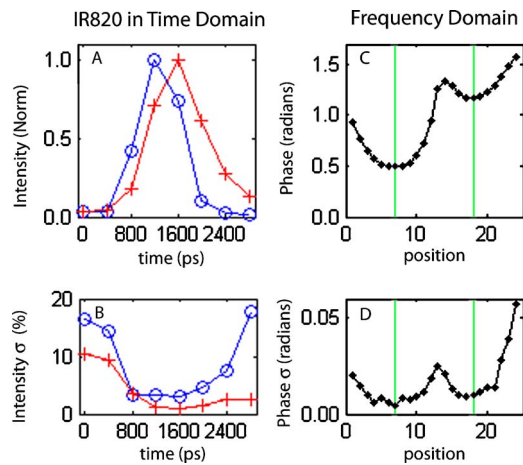
Fig. 2 Time-domain acquisition for a single source [(a) and (b)] and frequency domain data for 24 opposing source-detector pairs [(c) and (d)]. (a) Time-domain data for a single opposing source-detector pair centered on the position of a cylindrical fluorescent target (IR820). The excitation measurement (circles) and emission measurement (crosses) values are the mean across 15 scans and normalized to a maximum intensity of unity. An offset of 400 ps between the excitation and emission mean times of flight is evident. (b) The corresponding standard deviation across 15 scans in intensity as a percentage of the mean signal. At all points with significant signal (>5% maximum), the standard deviation is <10%. (c) The phase shift (in radians) between the emission and excitation data from a horizontal line of 24 opposing source-detectors at a virtual frequency of 210 MHz. The approximate horizontal location of the tubes is shown by green lines. The tube on the left with a faster lifetime (IR820) shows a phase offset nearly 0.7 radians shorter than the tube on the right with a longer lifetime (DTCCI). (d) Standard deviation in phase shift measurements. Deviation values amount to less than 1% of the phase offset at tube locations. (Color online only.)

D-phenylalanine). RGD is the arginine-glycine-aspartate motif, known to exhibit high affinity for the alpha-v-beta-3 integrin receptor (ABIR).[19] 4T1 murine mammary carcinoma tumors were grown in the right flank of a nude mouse by subcutaneous injection of 2×10^5 cells. ABIR is overexpressed by endothelial cells of new blood vessels and by many types of cancer cells,[20] including the 4T1 tumors used in this experiment.[21] When the tumor had grown to about 10 mm diameter, the mouse was anesthetized with isoflurane gas and then cypate-cycloRGDfK (1 mg/kg) was injected via the lateral tail vein. Scans were taken 24 h post-injection. We scanned 8 time-gates with 16 lateral by 12 vertical source positions with 3-mm separation. The total acquisition time was just under 3 min and 14 min for excitation and emission, respectively.

3 Experimental Results

3.1 *Phantom*

In the time domain, the FLT-DOT system reproducibly captures the excitation and emission pulses. This is best illustrated in the mean time-course for a single source-detector (SD) pair centered on the IR820 tube [Fig. 2(a)]. At this location, the excitation pulse clearly precedes the emission by about 400 ps, consistent with our expectation of a reconstructed lifetime below 500 ps. The deviation between 15 re-
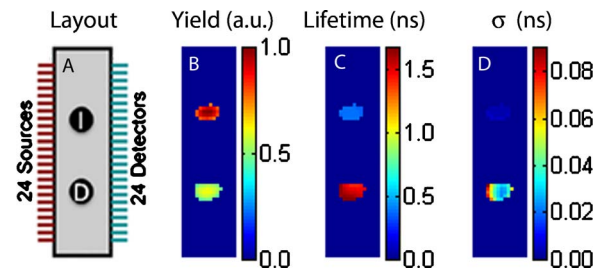
Fig. 3 Reconstructed lifetime and yield for tube phantoms. (a) Diagram of the fluorescence phantom and measurement geometry. 24 source positions with 2-mm separation are indicated with their opposing detector positions. The target with IR820 (top) is expected to have a lifetime below 500 ps, while the target with DTCCI (bottom) is expected to have a lifetime above 1000 ps. (b) Yield images (with >50% threshold) locate both targets. (c) Lifetime images further characterize the tubes, where IR820 (top) $\tau = 349 \pm 4$ ps (mean±standard deviation), and DTCCI (bottom) $\tau = 1273 \pm 39$ ps. (d) A voxel-wise mapping of the standard deviation in lifetime over 15 scans. IR820 was stable throughout the experiment, whereas DTCCI exhibited decreased activity in repeated scans. The lifetime deviation at the voxel level is low, amounting to less that 5% for most points.

peated measurements at each point in the time-course [Fig. 2(b)] demonstrates the high precision in our acquisition. For all points with signal >5% of maximum, the deviation is <9% for excitation and <4% for emission.

In the frequency domain, the delay in emission (the fluorescence lifetime) appears as a phase shift. A row of 24 opposing SD pairs illustrates this lifetime influence when coupled with fluorophore location [Fig. 2(c), $\omega = 210$ MHz]. At the tube locations, denoted by green bars, the shift for the IR820 (left) is nearly 0.7 radians smaller than that for DTCCI (right). At 210 MHz, this 0.7 radian shift denotes a lifetime delta in excess of 500 ps in the raw point sources (prior to diffuse modeling), consistent with the lifetimes of our fluorophores in organic solvents.[22] For SD pairs farther from the tube location, the phase shift increases. At these points, the emission measurement involves excitation light that must travel laterally to reach the tubes and emission light that must travel laterally back to the detector. The transmitted excitation meanwhile travels primarily straight from source to detector. The increased phase shift away from the tubes reflects this difference in total path length. Phase measurements are precise for both dyes, with the deviation [Fig. 2(d)] amounting to less than 1% of the phase shift at the tube locations.

A horizontal slice from the tomographic reconstruction demonstrates the fidelity of the FLT-DOT imaging (Fig. 3). We provide a diagram of the tube arrangement along with source and detector positions for reference [Fig. 3(a)]. The fluorescence yield serves as a threshold (yield > than 50% of tube maximum) to identify our tubes in the reconstruction. The voxel mean (over 15 scans) of yield and lifetime [Figs. 3(b) and 3(c), respectively] from the resulting regions show good spatial agreement with the diagram. The tube with IR820 (top) has $\tau = 349 \pm 4$ ps (mean ± standard deviation), while DTCCI (bottom) has $\tau = 1273 \pm 39$ ps. The low deviation in this lifetime on a per-voxel basis [Fig. 3(d)] demonstrates the reconstruction stability and measurement reproducibility (10 ART iterations for each reconstruction). Deviation
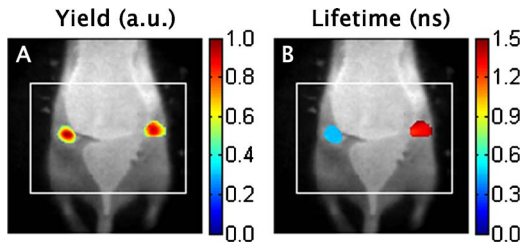
Fig. 4 *In vivo* validation using dye-loaded implants. (a) Fluorescence yield for gelatin implants as an overlay on a white-light image of the mouse to indicate position (a vertical slice from a 3-D image with a threshold at >50% of maximum). The box outline (white) indicates the scanned region. (b) The co-registered fluorescence lifetime for the gelatin implants (an equivalent vertical slice from a 3-D image of fluorescence lifetime). The mean lifetimes are cypate (left) τ =0.47 ns and DTCCI (right) τ=1.34 ns. External confirmation of the same targets measured cypate τ=0.47 ns and DTCCI τ=1.25 ns.

Fig. 5 *In vivo* targeted probe with tumor. (a) Fluorescence yield for a mouse with a tumor, imaged 24 h postinjection of a targeted agent (cypate-cyclic[RGDfK]; a vertical slice at 8 mm depth from a 3-D image). The subcutaneous tumor is evident on the right flank along with accumulation in the liver. (b) Co-registered fluorescence lifetime (an equivalent vertical slice from a 3-D image of fluorescence lifetime). The tumor region lifetime is near $\tau \approx 0.6$ ns, typical for cypate dyes in intralipid.

in the IR820 tube is below 10 ps at each point, while the bulk of the DTCCI tube is below 50 ps.

3.2 Scanned Mice with Implants

Vertical slices, at a depth of 4 mm from the detection plane, from a 3-D reconstruction of yield (η) and lifetime (τ), are shown in Fig. 4 for the mouse with NIR dye-gel implants. The thresholded (>50% maximum yield) yield information is superimposed on a white-light image [Fig 4(a)] to indicate relative position of the targets. The white box indicates the region scanned during the experiment. From the yield image, it is evident that the total signal from each of the implants was nearly equivalent. On the other hand, the lifetime data clearly discriminates the two tubes, with cypate on the left and DTCCI on the right [Fig 4(b)]. The mean reconstructed *in vivo* lifetimes and the external measurements taken just prior to implantation are close, with τ_{Cypate}=0.47 ns and τ_{DTCCI} =1.34 ns *in vivo* compared to τ_{Cypate}=0.47 ns and τ_{DTCCI} =1.25 ns externally.

3.3 Scanned Mice with Tumor

Twenty-four hours after injection with a peptide (cyclic RGD)–targeted NIRF probe, the mouse with subcutaneous 4T1 tumor exhibits accumulation in the tumor, kidneys, and liver. A vertical slice at 8 mm depth (center of the reconstruction) shows the signal from these tissues (Fig. 5). To assist with recognition, we exclude regions, with yield below 30% of the slice maximum and overlay this information on the white-light image of the mouse. Two primary regions are evident in the yield image [Fig. 5(a)]. In the upper-left region, the signal from the liver is visible. The region to the right displays the signal from the tumor with some overlap from the right kidney at the top. The lifetime for the same regions [Fig. 5(b)] shows a range from about 0.5 ns to 0.8 ns. The center of the liver lobe displays a value lower than the rest of the liver, while the tumor has an average lifetime near 0.6 ns.

4 Discussion

4.1 Demonstrations

4.1.1 Phantoms show range and repeatability

As demonstrated by our phantom experiment, we are able to simultaneously measure a reasonable range of lifetimes between 349 and 1273 ps. Moreover, repeated measurements have an error envelope typically within 6% (Fig. 2). Based on these error measurements in phantoms and the limits of our hardware, we can estimate the feasible lifetime range of our system. The upper limit can be estimated by considering the repetition rate of our laser system (80 MHz with pulses 12.5-ns apart) and our delay unit, which can measure out to 50 ns. Allowing for measurements of the pulse rise and fall, a fluorescence lifetime of up to 6 ns should be easily accommodated by the current system arrangement. Here, we allow for the larger phase delays for source-detector measurements not centered on the dye location. The lower limit can be estimated by considering the standard deviation in the reconstructed lifetimes. For the two tubes, we had standard deviations across scans from 4 ps to 39 ps for IR820 and DTCCI, respectively. A conservative limit for minimum lifetime is thus 50 ps, which is fast compared to previous *in vivo* lifetime measurements.[3]

4.1.2 In vivo lifetimes can be measured accurately

The agarose implants provide a controlled fluorescent source in which we can directly compare *in vivo* and *ex vivo* results. They also allow us to test the hypothesis that fluorescence lifetime imaging can be performed in the presence of heterogeneous optical properties and natural small animal respiratory motions. Despite these additional challenges, the system recovers the lifetimes within 10% of their conventional measurements. This reasonable error is typical for *in vivo* experiments. As with the phantoms, the lifetime measurements are generally flat across the region of the implant. By comparison, the yield has the characteristic peak and fall off of a point-spread function.

Measurements in the preclinical cancer model show relatively high accumulation in the dye concentration in tumor, kidneys, and liver relative to other tissues, with some heterogeneity in lifetime. The lifetimes of cypate-based dyes are

known to depend on the polarity of the local environment.[22] Thus, heterogeneity in the lifetime image [Fig. 5(b)] may reflect heterogeneity in tissue polarity. Future studies can evaluate this aspect in more detail. The lifetimes recovered are well within the expected bounds for a cypate dye in a biological environment, with the average lifetime in the tumor matching the lifetime in intralipid.

4.2 *Previous FLT Imaging*

Previous *in vivo* FLT imaging has been primarily reported using an FLT planar reflectance imaging (FLT-PRI) geometry. The pioneering work by Cubeddu et al.[23–26] with planar illumination and a gated image intensifier demonstrated the use of FLTs to discriminate cancerous and noncancerous tissue based on intrinsic autofluorescence contrast. These studies used visible excitation wavelengths where autofluorescence signals are much higher than in the NIR (700 to 900 nm) wavelengths. *In vivo* FLT-PRI of exogenous contrast agents has also been demonstrated.[24,27] However, the FLT-PRI geometry used in these examples has several significant limitations. Due to strong light scattering by tissues (the optical mean free path is $\sim 100~\mu$m, and the optical transport mean free path is ~ 1 mm), FLT-PRI exhibits a rapid falloff in sensitivity with increasing depth. Superficial structures (absorbing, scattering, or fluorescing) further obscure subsurface tissue structures.

An alternative method, FLT raster scan imaging (FLT-RSI), which scans a single source and detector pair with time-resolved detection, has also been reported.[28] Most recently, we used a commercial FLT-RSI system (eXplore Optix, GE Healthcare Technologies, Waukesha, Wisconsin) to image a targeted probe in tumors and internal organs.[29] FLT-RSI has an advantage in increased sensitivity to deeper tissues over FLT-PRI; however, the reflection mode geometry used is not optimal for generating robust sectioned and quantitative whole-body mouse images.[6,7] The practical drawbacks remain a lack of true 3-D tomographic sectioning and the obstruction of deeper tissues (e.g., FLT-labeled tumor tissues) by signals from superficial contrasts (e.g., autofluorescence). Furthermore, the mean time of flight of the fluorescence signals is used for depth profiling.[28] Thus, the lifetime is recovered from only the decay portion of the temporal point-spread function, which due to deconvolution issues, limits reliable FLT measurements to FLTs >500 ps.

DOT methods for whole-body animal imaging discussed herein are designed to address the limitations of planar reflectance imaging and raster scanning methods.[4,9,11,30] In extending *in vivo* DOT to FLT contrasts, both frequency-domain and time-domain approaches are possible. The frequency-domain approach has the algorithmic advantage that a linear solution can be obtained.[4] The full time-domain approach is more complex, is less tractable, and involves integration of the spatiotemporal excitation profile and the spatiotemporal propagation of the fluorescence emission.[31,32] Thus, most simulated tomography studies have used frequency-domain approaches.[33–36] Experimental 3-D, frequency-domain FLT tomography has been demonstrated for data at <100 MHz and phantom measurements.[37]

4.3 *Design Choices*

A significant feature of our FLT-DOT design is the measure of lifetime via phase shift following Oleary et al.[4] Effectively, we are measuring the change in the mean time of flight between excitation and emission photons. This is in contrast to other recent *in vivo* approaches that fit the slope of the temporal decays of emission data.[12,32] Conceptually, our solution uses a lower order moment of the data (mean value rather than slope of the temporal distribution) and thus is, in principle, a more robust measurement. Experimentally, the phase shift approach results in lifetime measurements with high precision (variance between scans) and accuracy (error from external confirmation). Furthermore, the phase shift measurement does not require a measurement of the instrument response function, as is typically required in time-domain acquisition. Moreover, the use of ratio-metric data (which takes the form of normalization in our reconstruction) helps account for inhomogeneous optical properties.

Employing time-domain acquisition with conversion to frequency-domain data for reconstruction is also a useful feature. Time-domain acquisition opens the possibility of greater dynamic control over the sources. While multiple images are required to build up the time curve (and thus the frequency-domain phase), this approach captures multiple frequencies in the process. For reconstruction, we have modified the general Born solution in the frequency domain to maintain simultaneous yield and lifetime reconstructions, while now incorporating normalization by the excitation measurements. While we do not detail the uses of multiple frequencies, the FLT-DOT system presented here acquires these measurements, as demonstrated in our previous publication.[2]

Another feature of our FLT-DOT system is the transmission geometry with a galvo-scanned source and a lens-coupled intensified CCD (ICCD). The spatial flexibility afforded by this source-detector arrangement is demonstrated throughout the experiments. For the symmetric tube phantom, we need only scan a strip across the target, while we can expand this area for *in vivo* mouse imaging. Ideal source-detector positioning and density have been discussed elsewhere, and we will not investigate them further here.[6,7,30] The transmission geometry provides a more even depth profiling than found with reflectance. This uniform profile allows for more accurate reconstruction and reduces the otherwise surface-weighted autofluorescence. While temporal and spectral approaches can also be used to reduce autofluorescence, the use of DOT measurement geometry to reduce autofluorescence allows the spectral and temporal data axes to be used for other purposes, including more efficient multiplexing of multiple probes.

5 Conclusions

FLT contrast provides a second contrast mechanism independent to fluorescence yield, and the addition of FLT to DOT increases the power of DOT as an *in vivo* diagnostic tool. The FLT-DOT system presented in this paper provides robust *in vivo* FLT measurements while maintaining the fast and flexible scanning of our previous fluorescence DOT platform.[2,9] Through a progressive series of experiments, we have shown that the FLT-DOT system presented measures FLT contrasts accurately and precisely and performs well both *in vitro* and

in vivo. We directly measured imaging agents with lifetimes from 349 to 1340 ps and, through noise analysis, predict a lower FLT limit below 50 ps. FLT images show good repeatability, with FLT values typically within 6% standard deviation, with an accuracy within 10% of conventional external measurements. We look forward to this FLT-DOT system design being used in conjunction with an emerging group of engineered NIR fluorescence molecular probes for application in a wide range of small animal imaging studies.

References

1. K. Suhling, P. M. W. French, and D. Phillips, "Time-resolved fluorescence microscopy," *Photochem. Photobiol. Sci.* **4**(1), 13–22 (2005).
2. S. V. Patwardhan and J. P. Culver, "Quantitative diffuse optical tomography for small animals using an ultrafast gated image intensifier," *J. Biomed. Opt.* **13**(1), 011009 (2008).
3. R. Cubeddu, D. Comelli, C. D'Andrea, P. Taroni, and G. Valentini, "Time-resolved fluorescence imaging in biology and medicine," *J. Phys. D* **35**(9), R61–R76 (2002).
4. M. A. Oleary, D. A. Boas, X. D. Li, B. Chance, and A. G. Yodh, "Fluorescence lifetime imaging in turbid media," *Opt. Lett.* **21**(2), 158–160 (1996).
5. I. Gannot, I. Ron, F. Hekmat, V. Chernomordik, and A. Gandjbakhche, "Functional optical detection based on pH dependent fluorescence lifetime," *Lasers Surg. Med.* **35**(5), 342–348 (2004).
6. B. W. Pogue, T. O. McBride, U. L. Osterberg, and K. D. Paulsen, "Comparison of imaging geometries for diffuse optical tomography of tissue," *Opt. Express* **4**(8), 270–286 (1999).
7. J. P. Culver, V. Ntziachristos, M. J. Holboke, and A. G. Yodh, "Optimization of optode arrangements for diffuse optical tomography: a singular-value analysis," *Opt. Lett.* **26**(10), 701–703 (2001).
8. J. P. Culver, R. Choe, M. J. Holboke, L. Zubkov, T. Durduran, A. Slemp, V. Ntziachristos, B. Chance, and A. G. Yodh, "Three-dimensional diffuse optical tomography in the parallel plane transmission geometry: evaluation of a hybrid frequency domain/continuous wave clinical system for breast imaging," *Med. Phys.* **30**(2), 235–247 (2003).
9. S. V. Patwardhan, S. R. Bloch, S. Achilefu, and J. P. Culver, "Time-dependent whole-body fluorescence tomography of probe biodistributions in mice," *Opt. Express* **13**(7), 2564–2577 (2005).
10. E. E. Graves, J. Ripoll, R. Weissleder, and V. Ntziachristos, "A sub-millimeter resolution fluorescence molecular imaging system for small animal imaging," *Med. Phys.* **30**(5), 901–911 (2003).
11. V. Ntziachristos and R. Weissleder, "Experimental three-dimensional fluorescence reconstruction of diffuse media by use of a normalized Born approximation," *Opt. Lett.* **26**(12), 893–895 (2001).
12. W. Akers, F. Lesage, D. Holten, and S. Achilefu, "*In vivo* resolution of multiexponential decays of multiple near-infrared molecular probes by fluorescence lifetime-gated whole-body time-resolved diffuse optical imaging," *Mol. Imaging* **6**(4), 237–246 (2007).
13. Y. P. Ye, S. Bloch, B. G. Xu, and S. Achilefu, "Design, synthesis, and evaluation of near infrared fluorescent multimeric RGD peptides for targeting tumors," *J. Med. Chem.* **49**(7), 2268–2275 (2006).
14. S. Achilefu, R. B. Dorshow, J. E. Bugaj, and R. Rajagopalan, "Novel receptor-targeted fluorescent contrast agents for *in vivo* tumor imaging," *Invest. Radiol.* **35**(8), 479–485 (2000).
15. M. S. Patterson, B. Chance, and B. C. Wilson, "Time-resolved reflectance and transmittance for the noninvasive measurement of tissue optical properties," *Appl. Opt.* **28**, 2331–2336 (1989).
16. R. C. Haskell, L. O. Svaasand, T. T. Tsay, T. C. Feng, and M. S. McAdams, "Boundary-conditions for the diffusion equation in radiative-transfer," *J. Opt. Soc. Am. A* **11**(10), 2727–2741 (1994).
17. A. C. Kak and M. Slaney, *Principles of Computerized Tomographic Imaging*, IEEE Press, New York (1988).
18. Y. Ye, S. Bloch, J. Kao, and S. Achilefu, "Multivalent carbocyanine molecular probes: synthesis and applications," *Bioconjugate Chem.* **16**(1), 51–61 (2005).
19. S. Achilefu, S. Bloch, M. A. Markiewicz, T. Zhong, Y. Ye, R. B. Dorshow, B. Chance, and K. Liang, "Synergistic effects of light-emitting probes and peptides for targeting and monitoring integrin expression," *Proc. Natl. Acad. Sci. U.S.A.* **102**(22), 7976–7981 (2005).
20. S. Zitzmann, V. Ehemann, and M. Schwab, "Arginine-glycine-aspartic acid (RGD)-peptide binds to both tumor and tumor-endothelial cells *in vivo*," *Cancer Res.* **62**(18), 5139–5143 (2002).
21. Z. Mi, H. Guo, P. Y. Wai, C. Gao, and P. C. Kuo, "Integrin-linked kinase regulates osteopontin-dependent MMP-2 and uPA expression to convey metastatic function in murine mammary epithelial cancer cells," *Carcinogenesis* **27**(6), 1134–1145 (2006).
22. M. Y. Berezin, H. Lee, W. Akers, and S. Achilefu, "Near infrared dyes as lifetime solvatochromic probes for micropolarity measurements of biological systems," *Biophys. J.* **93**(8), 2892–2899 (2007).
23. R. Cubeddu, R. Ramponi, P. Taroni, and G. Canti, "Time-gated fluorescence spectroscopy of porphyrin derivatives and aluminum phthalocyanine incorporated *in vivo* in a murine ascitic tumor-model," *J. Photochem. Photobiol., B* **11**(3–4), 319–328 (1991).
24. R. Cubeddu, P. Taroni, and G. Valentini, "Time-gated imaging-system for tumor-diagnosis," *Opt. Eng.* **32**(2), 320–325 (1993).
25. R. Cubeddu, P. Taroni, G. Valentini, F. Ghetti, and F. Lenci, "Time-gated fluorescence imaging of blepharisma red and blue cells," *Biochim. Biophys. Acta* **1143**(3), 327–331 (1993).
26. R. Cubeddu, A. Pifferi, P. Taroni, G. Valentini, and G. Canti, "Tumor detection in mice by measurement of fluorescence decay time matrices," *Opt. Lett.* **20**(24), 2553–2555 (1995).
27. J. S. Reynolds, T. L. Troy, R. H. Mayer, A. B. Thompson, D. J. Waters, K. K. Cornell, P. W. Snyder, and E. M. Sevick-Muraca, "Imaging of spontaneous canine mammary tumors using fluorescent contrast agents," *Photochem. Photobiol.* **70**(1), 87–94 (1999).
28. D. Hall, G. B. Ma, F. Lesage, and W. Yong, "Simple time-domain optical method for estimating the depth and concentration of a fluorescent inclusion in a turbid medium," *Opt. Lett.* **29**(19), 2258–2260 (2004).
29. S. Bloch, F. Lesage, L. McIntosh, A. Gandjbakhche, K. X. Liang, and S. Achilefu, "Whole-body fluorescence lifetime imaging of a tumor-targeted near-infrared molecular probe in mice," *J. Biomed. Opt.* **10**(5), 054003 (2005).
30. E. E. Graves, J. P. Culver, J. Ripoll, R. Weissleder, and V. Ntziachristos, "Singular-value analysis and optimization of experimental parameters in fluorescence molecular tomography," *J. Opt. Soc. Am. A* **21**(2), 231–241 (2004).
31. D. Hattery, V. Chernomordik, M. Loew, I. Gannot, and A. Gandjbakhche, "Analytical solutions for time-resolved fluorescence lifetime imaging in a turbid medium such as tissue," *J. Opt. Soc. Am. A* **18**(7), 1523–1530 (2001).
32. A. T. N. Kumar, S. B. Raymond, G. Boverman, D. A. Boas, and B. J. Bacskai, "Time-resolved fluorescence tomography of turbid media based on lifetime contrast," *Opt. Express* **14**(25), 12255–12270 (2006).
33. D. Y. Paithankar, A. U. Chen, B. W. Pogue, M. S. Patterson, and E. M. Sevick-Muraca, "Imaging of fluorescent yield and lifetime from multiply scattered light reemitted from random media," *Appl. Opt.* **36**(10), 2260–2272 (1997).
34. H. B. Jiang, "Frequency-domain fluorescent diffusion tomography: a finite-element-based algorithm and simulations," *Appl. Opt.* **37**(22), 5337–5343 (1998).
35. F. Fedele, J. P. Laible, and M. J. Eppstein, "Coupled complex adjoint sensitivities for frequency-domain fluorescence tomography: theory and vectorized implementation," *J. Comput. Phys.* **187**(2), 597–619 (2003).
36. A. B. Milstein, J. J. Stott, S. Oh, D. A. Boas, R. P. Millane, C. A. Bouman, and K. J. Webb, "Fluorescence optical diffusion tomography using multiple-frequency data," *J. Opt. Soc. Am. A* **21**(6), 1035–1049 (2004).
37. A. Godavarty, E. M. Sevick-Muraca, and M. J. Eppstein, "Three-dimensional fluorescence lifetime tomography," *Med. Phys.* **32**(4), 992–1000 (2005).